Receiver function mapping of the mantle transition zone beneath the Western Alps: New constraints on slab subduction and mantle upwelling

Dongyang Liu, Liang Zhao, Anne Paul, Huaiyu Yuan, Stefano Solarino, Coralie Aubert, Silvia Pondrelli, Simone Salimbeni, Elena Eva, Marco G Malusà, et al.

Receiver function mapping of the mantle transition zone beneath the Western Alps: New constraints on slab subduction and mantle upwelling

Dongyang Liu[a,b], *Liang Zhao*[a,b,*], *Anne Paul*[c], *Huaiyu Yuan*[d,e], *Stefano Solarino*[f], *Coralie Aubert*[c], *Silvia Pondrelli*[g], *Simone Salimbeni*[g], *Elena Eva*[f], *Marco G. Malusà*[h,f], *Stéphane Guillot*[c]

[a] State Key Laboratory of Lithospheric Evolution, Institute of Geology and Geophysics, Chinese Academy of Sciences, Beijing 100029, China

[b] College of Earth and Planetary Sciences, University of Chinese Academy of Sciences, Beijing 100049, China

[c] Univ. Grenoble Alpes, Univ. Savoie Mont Blanc, CNRS, IRD, UGE, ISTerre, 38000 Grenoble, France

[d] ARC Centre of Excellence for Core to Crust Fluid Systems, Department of Earth and Environmental Sciences, Macquarie University, North Ryde, Australia

[e] Centre for Exploration Targeting, School of Earth Sciences, The University of Western Australia, 35 Stirling Highway, Crawley, Perth, Western Australia 6009, Australia

[f] Istituto Nazionale di Geofisica e Vulcanologia, Osservatorio Nazionale Terremoti, Genova, Italy

[g] Istituto Nazionale di Geofisica e Vulcanologia, Via Donato Creti 12, 40128 Bologna, Italy

[h] Department of Earth and Environmental Sciences, University of Milano-Bicocca, Milan, Italy

*Corresponding author at: State Key Laboratory of Lithospheric Evolution, Institute of Geology and Geophysics, Chinese Academy of Sciences, Beijing 100029, China

E-mail address: zhaoliang@mail.iggcas.ac.cn (L.Zhao)

Abstract[1]

To better constrain the deep structure and dynamics of the Western Alps, we studied the mantle transition zone (MTZ) structure using P-wave receiver functions (RFs). We obtained a total of 24904 RFs from 1182 events collected by 307 stations in the Western Alps. To illustrate the influence of the heterogeneity on the upper mantle velocity, we used both IASP91 and three-dimensional (3-D) velocity models to perform RF time-to-depth migration. We documented an MTZ thickening of about 40 km under the Western Alps and most of the Po Plain due to the uplift associated with the 410-km discontinuity and the depression associated with the 660-km discontinuity. Based upon the close spatial connection between the thickened MTZ and the location of the subducted slabs, we proposed that the thick MTZ was due to the subduction of the Alpine slab through the upper MTZ and the presence of remnants of subducted oceanic lithosphere in the MTZ. The uplift associated with the 410-km discontinuity provided independent evidence of the subduction depth of the Western Alps slab. In the Alpine foreland in eastern France, we observed localized arc-shaped thinning of the MTZ caused by a 12 km depression of the 410-km discontinuity, which has not been previously reported. This depression indicated a temperature increase of 120 K in the upper MTZ, and we proposed that it was caused by a small-scale mantle upwelling. Hardly any uplift of the 660 km discontinuity was observed, suggesting that the thermal anomaly was unlikely to be the result of a mantle plume. We observed that the thinning area of the MTZ corresponded to the area with the highest uplift rate in the

[1]**Abbreviations**

mantle transition zone (MTZ)

receiver function (RF)

common conversion point (CCP)

Western Alps, which may have indicated that the temperature increase caused by the mantle upwelling contributed to the topographic uplift.

Keywords: Mantle transition zone, Subduction zone processes, Western Alps, Mantle processes, Receiver functions.

1 INTRODUCTION

The mantle transition zone (MTZ) separates the upper mantle from the lower mantle over the entire Earth. The MTZ has been widely studied because the topography of its upper and lower boundaries inferred from geophysical observations can be linked to the results of mineral physics in terms of the thermal state, mineralogy and/or water content of the transition zone. Subducting plates and mantle convection induce phase transitions at the upper (410-km) and lower (660-km) boundaries of the MTZ in the form of thermal perturbations, which can be traced as depth changes in these discontinuities. Such depth variations provide clues to the structure and dynamics of the upper mantle. The subduction depth of the Western Alps slab and the origin of the mantle flow beneath and inside the mantle lid of the European Plate play crucial roles in our understanding of the regional geodynamics. The rapid topographic uplift rates in the Western Alps are believed to be partly due to mantle-related processes (Serpelloni et al., 2013; Nocquet et al., 2016; Sternai et al., 2019). Therefore, we used receiver functions (RFs) to study the seismic characteristics of the MTZ under the Western Alps, to provide new constraints on the depth penetration of the subducted plate, and then discuss the geodynamic origin of the low-velocity anomaly behind the subduction zone and its relationship with the present-day uplift rates in the Western Alps.

1.1 MTZ under the Western Alps and adjacent areas

The MTZ is bound by two global scale discontinuities at depths of 410 km and 660 km, characterized by strong seismic velocity changes, which are mainly related to high-pressure phase transitions of olivine in seismic properties. The 410-km discontinuity is associated with the polymorphic phase transitions from olivine (α spinel) to wadsleyite (β spinel) in an exothermic reaction with a positive Clapeyron slope. The 660-km discontinuity is associated with phase transitions from ringwoodite (γ spinel) to bridgmanite and ferropericlase, in an endothermic reaction with a negative Clapeyron slope. Therefore, a 100 K temperature decrease in the MTZ induced the uplift of the 410-km discontinuity and the depression of the 660-km discontinuity, and thus, about 10 km of thickening. Conversely, a thinner MTZ is expected in anomalously hot regions. Lateral variations in the depths of the two seismic discontinuities provide important information about the lateral temperature variations within the MTZ, and therefore, they can be used to constrain the geometric characteristics of subducted plates and reflect the scale of mantle convection.

Van der Meijde et al. (2005) studied the MTZ structure beneath a sparse station array in the Mediterranean region using RFs. The only station they used in the Alps was in the southwestern part of the belt. It revealed a thick MTZ, which Van der Meijde et al. (2005) explained as high average seismic velocities in the MTZ. Lombardi et al. (2009) used data from 98 stations spread over the Alpine region and reported an increase in the thickness of the MTZ of about 30–40 km in a large zone covering the southwestern Alps and most of the Po Basin. Because this thickness anomaly is due only to a subsidence of the 660-km discontinuity, Lombardi et al. (2009) proposed that the 40 km of thickening was due to a strong temperature decrease of about 800 K in the lower part of the MTZ. They attributed this cold anomaly to the presence of lithospheric slab remnants from the Tethyian Ocean, which accumulated at the 660-km discontinuity. The European-scale study of Cottaar and Deuss (2016) revealed large-scale 30 km depressions of the 660-km discontinuity beneath central Europe, without any corresponding topographic variation in the 410-km discontinuity. Although they had good station coverage in the Alpine area, their results did not confirm the strong anomaly in the 660-km discontinuity reported by Lombardi et al. (2009) in the Western and Southern Alps. Liu et al. (2018) focused their RF analysis on the Alpine region to investigate water transport through the MTZ in subduction zones. They suggested that the 660-km discontinuity was depressed by 10–40 km beneath the south-central Alps, whereas the 410-km discontinuity was not deflected appreciably. Liu et al. (2018) proposed that the depressed 660-km discontinuity indicated that the subducted material had sunk to the bottom of the transition zone. They also provided evidence of low-velocity zones (LVZs) above the 410-km discontinuity beneath the regions near the Alpine subduction, such as northeastern France and the Ligurian Sea. According to Liu et al. (2018), these LVZs outside of the Alps could be explained by melting induced by water released from the MTZ in an ascending mass flow that compensated for the descending flow caused by the spreading of the lithospheric slab remnants above the 660-km discontinuity.

In this study, we used a much denser seismic array than those used in previous studies, including permanent and temporary stations of the CIFALPS and CIFALPS-2 experiments (see improvement in the mapping of the 410-km discontinuity in Fig. S1). In addition, we used a three-dimensional (3-D) velocity model to calculate accurate ray paths and to correct the depth estimates of the MTZ discontinuities in the structure of the upper mantle. The results of our study provides new constraints and shed light on the topographic variations in the two discontinuities over a broad region, including the Western Alps and the Alpine foreland in Eastern France.

1.2 Tectonic background

The Alpine orogenic belt is the result of continental collision and convergence between the Adriatic microplate and the European Plate during the Mesozoic (Handy et al., 2010). During the Cretaceous, most of the Tethys Ocean subducted below the Adriatic Plate (Dewey et al., 1989; Malusà et al., 2015). With the progressive closure of the Tethys Ocean, subduction was blocked in the Middle-Late Eocene. The Apenninic slab gradually moved northward and may have started interacting with the European Plate from the Oligocene (Malusà et al., 2016). The Apenninic Plate retreated eastward in the Neogene, resulting in the opening of the Ligurian sea (Jolivet and Faccenna, 2000) and the associated counterclockwise rotation of Corsica-Sardinia in the Apenninic backarc region (Fig. 1) (Lustrino et al., 2011). The Alpine orogenic belt has a complex tectonic history, and the deformation in and around the Alps is controlled by the displacements of several microplates (e.g., Adria and Iberia), which generated orogenic belts around the Alps, particularly the Pyrenees, the Apennines, the Betics, and the Dinarides (Handy et al., 2010).

The seismic velocity anomalies in the mantle beneath the Western Alps have been analyzed using various tomography models (Piromallo and Morelli, 2003; Lippitsch et al., 2003; Koulakov et al., 2009; Zhu et al., 2012, 2015; Zhao et al., 2016a; Hua et al., 2017). Seismic tomography studies of the crust and upper mantle beneath the Western Alps have mapped a dipping slab that can be traced from the crust to the MTZ (e.g., Zhu et al., 2012; Zhao et al., 2016a; Hua et al., 2017). This high-velocity anomaly has been interpreted as the Alpine slab in all publications. Regional tomography results for the area beneath the central-western Mediterranean also revealed that a large amount of high-velocity materials has accumulated in the MTZ, which resulted from different subduction episodes (Piromallo and Morelli, 2003; Zhu et al., 2012). According to a preliminary interpretation of the recent teleseismic tomography data obtained by Paffrath et al. (2020), Agard and Handy (2021) proposed that the steeply dipping subducted slab is mostly of European origin and that a gap exists in-between the subducted lithosphere with strong dip and the slab remnants in the MTZ on the 660-km discontinuity. A low-velocity anomaly was imaged from 100 km to 250 km on the lower plate side of the Western Alps slab, extending with lower amplitudes down to the transition zone (e.g., Koulakov et al., 2009; Zhao et al., 2016a), which was attributed to thermal origin and may be linked to a counterflow induced by rollback of the Apenninic slab (Zhao et al., 2016a; Malusà et al., 2021). Hua et al. (2017) proposed that the high-velocity anomalies in the mantle under the Alps coexist with negative radial anisotropy, which could be triggered by a subducting slab and the mantle flow it induced. In the Western Alps, these mantle processes also may significantly contribute (~30%) to the observed surface uplift rates predicted by modeling of the dynamic topography (Sternai et al., 2019). Therefore, the Western Alps are an ideal location for studying the origin of the low-velocity anomaly behind the subduction zone and its influence on the topography. Indeed, low-velocity anomalies behind subduction zones have been observed not only in the Western Alps but also at the plate boundaries in Japan (Wei and Shearer, 2017) and in the Western United States (Bodmer et al., 2018).

2. Data and methods

We used waveform data collected from 307 broadband seismic stations in the Western Alps and adjacent foreland areas (Fig. 1b). In addition to the 197 stations that are part of the Swiss (CH), French (FR, RD, G), and Italian (IV, GU) permanent networks, we used data from 110 temporary stations set up for two experiments in the China-Italy-France Alps Seismic Survey (CIFALPS) project. Both the CIFALPS and CIFALPS-2 experiments included 55 stations spaced about 5–10 km apart along transects through the southwestern Alps for the CIFALPS and the northwestern Alps and the Ligurian Alps for CIFALPS-2. The CIFALPS stations operated for 13 months in 2012–2013 (Zhao et al., 2015, 2016b); and the CIFALPS-2 experiment operated for 14 months in 2018–2019 (Zhao et al., 2018). We selected events with epicentral distances of 30°-90° and magnitudes (Mw) of 5.3 to 9.0 for the period 2012–2019.

Assuming that the vertical component represents the source time function, we calculated the RFs using time-domain interactive deconvolution of the vertical component from the radial component (Ligorría and Ammon, 1999). The data were band pass filtered in the frequency band of 0.02–0.5 Hz and windowed from 15 s before to 100 s after the predicted direct P-wave arrival time. We employed an automatic screening criterion to select high-quality RFs: (1) the direct P arrival should be within 1s of the zero-delay time; and (2) after the main P-wave, there should not be another peak exceeding 70% of the P-wave amplitude. We calculated the correlation between each individual receiver function and the average receiver function at the given station and rejected the signals with correlation coefficients of less than 0.4. Then, the data were manually checked for quality. After the quality check, we kept 24904 RFs from 1182 teleseismic events for further analysis.

We used the common conversion point (CCP) stacking approach (Dueker and Sheehan, 1997) to construct a 3-D image of the RFs with depth to map the topographic variations in the two discontinuities. The CCP stacks were created using RFs from different sources and records from different stations, but they sampled the same target region at depth. Before the stacking, we divided the region under the Western Alps into small blocks (10 km × 10 km horizontally and 2 km in depth) from the surface to a depth of 800 km. For each conversion depth, we calculated the piercing points and travel times of the converted Ps (P to S) phase through ray tracing within a velocity model. We considered two reference velocity models, the IASP91 spherical Earth reference model (Kennett and Engdahl, 1991) and the EU60 3-D model (Zhu et al., 2015), to accurately locate the piercing points of the Ps phases and then to compute the moveout corrections. The EU60 model is a 3-D crust and upper mantle velocity model computed from adjoint tomography data, which constrains the absolute P-wave and S-wave velocities from the subsurface to a depth of 1000 km (Zhu et al., 2015). Because of the inclusion of body waves, the ray coverage of the EU60 model can be extended to the MTZ. The P-wave velocity variations at 410 km and 660 km and the Vp/Vs ratio at 600 km in the EU60 model are shown in Fig. 2. It is possible to observe the high-velocity anomalies below the Po Plain, a low-velocity anomaly around the orogenic belt at 410 km (Fig. 2a), and a high-velocity anomaly at 660 km (Fig. 2b). Similar anomalies have been imaged in other tomography studies (Piromallo and Morelli, 2003; Koulakov et al., 2009; Zhao et al., 2016a).

With the improvements in the accuracy and resolution of tomographic models, 3-D velocity models have been used to migrate RF data. To calculate the mantle corrections to the relative Ps travel times, we first computed the true 3-D ray paths based on the EU60 velocity model using the fast-marching method (Rawlinson et al., 2005). Then, we divided each ray into depth segments and calculated the travel time for each ray segment according to the EU60 model. The amplitudes of the RFs were back-projected to the grid points corresponding to the ray paths according to their relative arrival times and were stacked into nearby grid points using a weighting factor that depends on the half width of the Fresnel zone at the corresponding depth (Test. S1 in the Supporting Information). To check the validity of the method, we designed two 1-D synthetic tests by adding a 100 km thick layer with an anomalous velocity in the upper mantle and in the MTZ (Fig. S2). Then, we applied the 1-D and 3-D correction methods, and the results showed the discontinuities were well recovered by the 3-D velocity corrections. Fig. 3 shows the geographic layout of the piercing points of the Ps conversions at the two discontinuities obtained using the 3-D velocity model, which indicates that the coverage of the study region was good.

3 Results

In general, the Ps conversions from the two discontinuities were prominent in the cross sections of the CCP stacks obtained using the IASP91 model (Fig. S3). The depression of the 660-km was quite visible in all sections, and it gradually approached the average global depth toward the north (Test. S2). Both uplift and depression were observed in different areas of the 410-km discontinuity. The amplitudes of the converted P410s phase weaken significantly in the north part of the study area, where P410s became hard to detect.

Maps of the discontinuity's topography were drawn by picking the depths of the maximum amplitudes of the RFs within the respective depth ranges of 380–440 km and 630–710 km. We found that the average depths of the two discontinuities were 414±10.3 km and 673±5.9 km for the IASP91 model (Figs. 4a and 4b). Figs. 5a and 5b showed the topographies of the two discontinuities estimated using the IASP91 model. A striking feature of the topographic maps was the depressed 660-km discontinuity across the entire study area, which was suggested by the CCP profiles (Fig. S3). The most prominent depth anomaly was located in the southern part of the mountain belt, where the 660-km discontinuity was about 30 km deeper than normal. As proposed in previous studies, the depressed 660-km discontinuity may be related to the widespread accumulation of cold materials in the MTZ (Lombardi et al., 2009). In contrast, the 410-km discontinuity was depressed in a large area to the north and west of the mountain belt, while the discontinuity is uplifted by about 10 km to 20 km beneath the Po Plain (Fig. 5a).

Figs 5d and 5e showed the depth variations of the two discontinuities corrected using the EU60 3-D P- and S-wave absolute velocity model. After the 3-D velocity corrections, the average depths of the two discontinuities were found to be 412±9.3 km and 675±5.7 km (Figs. 4c and 4d). For most of the study area, overall, the depth changes of the discontinuities corrected using the EU60 velocity heterogeneities were similar to those corrected using the IASP91 model (Figs. 5a, 5b, 5d, 5e). The main difference was the absolute depth of the discontinuities. The depth of the depressed 410-km discontinuity was corrected by a maximum of 12 km, which was a result of accounting for the low-velocity anomaly in the tomography of the EU60 (Fig. 2a). Therefore, the topographic relief and the standard deviation on the depth of the 410-km discontinuity were smaller for the EU60 model than for the IASP91 model (Figs. 4a, 4c, 5a, and 5d). The depths of the 660-km discontinuity were greater after correction using the EU60 model, with a maximum correction of 5 km, which corresponded to the correction for the high-velocity anomalies in the MTZ (Fig. 2b). This depth correction was consistent with the velocity variations in the EU60 model. We calculated the standard errors on the depths of the discontinuities, which were less than 5 km in most areas (Fig. S4). Therefore, based on the good data coverage of our study (Figs. 3a and 3b) and the fair resolution of the EU60 model in the study area, we are confident that the depth variations of the two discontinuities were robustly estimated.

The thickness of the MTZ was obtained by subtracting the depth of the 410-km discontinuity from the depth of the 660-km discontinuity in overlapping CCP bins to eliminate uncertainties caused by migration using an inaccurate velocity model in the upper mantle. The MTZ thickness maps created using the IASP91 model and the EU60 model were similar (Figs. 5c and 5d). The most prominent anomaly was the thickening of the transition zone beneath the Western Alps and the Po Plain. The MTZ was approximately 25–40 km thicker than the global average of 250 km in the IASP91 Earth model, which corresponded to the locally depressed 660-km discontinuity and uplifted 410-km discontinuity shown in Figs. 5d and 5e. The 12 km (on average) thinning of the MTZ occurred in the Alpine foreland of Eastern France (Fig. 5f). These variations in the thickness were correlated with the velocity structure of the MTZ. The MTZ tended to be thicker where the velocities were higher, and thinner where the velocities were lower (Figs. 2a and 2b).

Fig. 6 compares the CCP stacked cross sections with the P-wave tomographic model of Zhao et al. (2016a) along the transects in the southwestern Alps (section a-A) and in the northwestern Alps (section b-B). In both cross sections, the depression of the 410-km discontinuity in the west correlated well with the low-velocity anomalies extending to the MTZ revealed by the P-wave tomography model. The high-velocity anomaly in the east matched the uplift of the 410-km discontinuity well.

4 Discussion

Using an accurate 3-D velocity model of the mantle should lead to more accurate estimates of the depths of two discontinuities and the thickness of the MTZ and thus to more accurate information about the temperature anomalies in the MTZ. In this section, we used the corrected depths of the discontinuities to constrain the subduction depth of the Western Alps slab, and we discussed the causes of the depression of the 410-km as well as the possible link between the mantle convection and topographic uplift.

4.1 Cold slabs in the MTZ beneath the Western Alps

The most salient anomaly in the MTZ was the 15–40 km increase in its thickness below the Western Alps and the Po Plain, with an average increase in thickness of about 28 km. The thickening of the MTZ was caused by the 10 km uplift of the 410-km discontinuity and the 30 km depression of the 660-km discontinuity. According to the synthetic test shown in Fig. S5, a 10-km anomaly could be identified from the RFs. In the following, we used Clapeyron slopes of +2.5 $MPa \cdot K^{-1}$ (Katsura and Ito, 1989) and -2.9 $MPa \cdot K^{-1}$ (Yu et al., 2007) for the 410-km and 660-km discontinuities, respectively. The 40 km thickening was related to a -300 K temperature anomaly in the MTZ as compared with the global average. Using the scaling parameter dVp/dT = -4.8×10^{-4} $km \cdot s^{-1} \cdot K^{-1}$ (Deal et al., 1999), the corresponding Vp anomaly in the MTZ was about +1.4%, which was in agreement with the high-velocity anomalies in the EU60 model (Fig. 2b). In addition, given that the depression of the 660-km discontinuity was the main reason for the thickening of the MTZ, we predicted a stronger temperature decrease of up to -450 K at the base of the MTZ, which would explain the 30 km depression of the 660-km discontinuity. This finding was consistent with the temperature decrease (350–450 K) in the MTZ inferred from deep magnetotelluric sounding data collected in the French Alps (Tarits et al., 2004).

Based upon the model corrected using the EU60, the uplifted 410-km discontinuity could be interpreted in terms of the low temperatures associated with the subducted Western Alps slab (Fig. 5d). Piromallo and Faccenna (2004) estimated that the convergence of Adria and Europe has resulted in at least 400 km of horizontal shortening in the Western Alps during the past 67 Ma according to plate-tectonic reconstruction results (Dewey et al., 1989). Zhu et al. (2012) suggested that the maximum subduction depth, revealed by their adjoint tomography model, is nearly 400 km beneath the Alpine belt. The teleseismic tomography of Zhao et al. (2016a) revealed a strongly dipping high-velocity anomaly that could be continuously traced to a depth of 400 km in the Western Alps, whereas a positive velocity anomaly of about +1% was still visible at a depth of ~420 km. Hua et al. (2017) suggested that the maximum depth of the subducted slab in the Western and Central Alps was ~450 to 500 km. The observed uplift of the 410-km discontinuity under the Western Alps may have indicated that the present-day subducted plate passed through the 410-km discontinuity and entered the MTZ (Figs. 5d and 6), providing an additional constraint on the maximum subduction depth of the Western Alps slab.

The depressed 660-km discontinuity indicated that cold subducted materials have accumulated at this discontinuity (Fig. 7). Tomographic images (Piromallo and Morelli, 2003; Zhu et al., 2012) have revealed a broad high-velocity zone in the MTZ in the Central-Western Mediterranean. Piromallo and Faccenna (2004) and Zhu et al. (2012) suggested that these large-scale anomalies may be pieces of the subducted Alpine Tethys oceanic lithosphere, which were conveyed to the MTZ by various subduction events and piled up at a depth of 660 km. Previous seismic studies of the MTZ under the Alpine region reported that the 660-km discontinuity was the only contributor to the thickening of the MTZ and was the only phase transition affected by the cold plate (Lombardi et al., 2009; Cottaar and Deuss, 2016; Liu et al., 2018). We have documented, however, that the uplifted 410-km discontinuity also contributed to the thickening of the MTZ. Therefore, the thicker transition zone beneath the Western Alps provided evidence not only of the presence of mantle lithosphere slab remnants above the 660-km discontinuity, as suggested by tomography studies (Piromallo and Morelli, 2003; Zhu et al., 2015), but also for the maximum depth reached by the high-velocity anomaly corresponding to the Alpine subduction.

In addition to temperature anomalies, a high-water content could also cause the thickening of the MTZ (Litasov et al., 2005). Studies have proposed that an increase in the water content of ringwoodite could reduce the Vs significantly, while having little effect on the Vp, and thereby increasing the Vp/Vs ratio (Jacobsen and Smyth, 2006). Seismic tomography studies have revealed an increase rather than a decrease in the S-wave velocity within the MTZ beneath the Western Alps (e.g., Utada et al., 2009; Zhu et al., 2015). Moreover, the Vp/Vs ratio does not increase at a depth of 600 km in the EU60 model (Fig. 2c) (Cottaar and Deuss, 2016). An increased water content also could broaden the depth interval of the phase transition, leading to an increase in the attenuation and low amplitude RFs (Wood, 1995). We did not observe, however, a decrease in the amplitude of the depressed 660-km discontinuity (Fig. S3). In addition, the electrical conductivity study conducted by Utada et al. (2009) revealed a low conductivity under the Mediterranean region at depths of 400–700 km, which correlated well with the high-velocity anomalies. Therefore, the hypothesis that the depression of the 660-km discontinuity was related to the widespread distribution of hydrous minerals was unlikely.

4.2 A hot MTZ surrounding the Western Alps slab

The map of the corrected MTZ thickness showed a thinner MTZ in the northwestern part of the Western Alps, which was caused mainly by the arc-shaped depression of the 410-km discontinuity around the arc-shaped Western Alps (Fig. 5). Because the 410-km discontinuity was more depressed than the 660-km discontinuity, the MTZ was 12 km thinner than the global average of 250 km, with a maximum thinning of 23 km. The depression of the 410-km discontinuity observed on the depth map corrected using the 3-D EU60 model (Fig. 5d) was not an artifact caused by an inaccurate velocity correction because it also was observed when the IASP91 1-D model was used for the migration (Fig. 5c). A low-velocity anomaly has been identified in various tomography studies of the area surrounding the Western Alps slab (Koulakov et al., 2009; Zhao et al., 2016a; Hua et al., 2017). New shear-wave splitting observations led Salimbeni et al. (2018) to propose that the low-velocity anomalies at the rear of the Western Alps slab have a thermal origin and may have generated the vertical component of the mantle counterflow induced by the retreat of the Apenninic slab to the south. The low-velocity anomalies can be traced from 100 km to 250 km depth and they extend with lower amplitudes down to the MTZ, which corresponded to the depressed 410-km discontinuity (e.g., Koulakov et al., 2009; Zhao et al., 2016a). The 12 km average thinning of the MTZ was mainly the results of the depressed 410-km discontinuity, which indicated a +120 K thermal anomaly at the 410-km discontinuity for a Clapeyron slope of +2.5 $MPa \cdot K^{-1}$. Using the scaling parameter $dVp/dT = -4.8 \times 10^{-4}\ km \cdot s^{-1} \cdot K^{-1}$ (Deal et al., 1999), the positive thermal anomaly led to a -0.6% velocity reduction, which was consistent with the results of previous seismic tomography studies (Koulakov et al., 2009; Zhu et al., 2015; Zhao et al., 2016a).

The slightly thinner MTZ caused by the larger depression of the 410-km compared with that of the 660-km discontinuity may have been due to the thermal anomaly in the upper part of the MTZ. It may represent small-scale mantle flow that would transport the hotter material of the MTZ into the upper mantle and induce a temperature increase. The depressed 410-km discontinuity was distributed outside of the Western Alps and parallel to the arc-shaped trend of the orogenic belt (Fig. 5d). We proposed that the mantle flow pattern at the rear of the Western Alps slab was composed of two components: (1) toroidal flow, that is, a counterflow induced by the Apenninic slab retreating to the southeast (Salimbeni et al., 2018; Malusà et al., 2021); and (2) poloidal flow and associated upwelling. The numerical simulations suggested that this upwelling usually was part of the return flow system caused by active slab subsidence (Faccenna et al., 2010). Therefore, a major cause of contributing to this thermal anomaly may be the downwelling of the Alpine lithosphere, which induced poloidal return flow in the surrounding mantle. On the basis of the observations that the Alpine subduction extended to the depth of the MTZ and that cold subducted materials accumulated in the MTZ at the 660-km discontinuity, the quasi-vertical Alpine subduction may have induced two poloidal flow cells, one underneath the subducting plate and the other one in the mantle wedge above the plate. This flow pattern would be caused by the shearing between the plate and the mantle because of the inclined plate parallel component of the displacement and could be better observed in vertical subduction (Schellart, 2004). Like the Western Alps, the thinning of the transition zone under the Pacific Coast of North America also was due to a more depressed 410-km as compared with the 660-km discontinuity, which indicated that the temperature in the upper part of the MTZ was higher (Gao and Liu, 2014). Bodmer et al. (2018) attributed the low-velocity anomaly along the Cascadia forearc to mantle upwelling and to a thermally buoyant mantle.

4.3 Relationship between topographic uplift and mantle upwelling

The Western Alps contain the highest peaks in Europe and have a higher average elevation than other segments of the Alpine orogen belt. However, the detailed mechanisms that control their surface uplift are not well understood. Global Positioning System (GPS) and leveling have revealed that the present-day uplift rates of the Alps are 1-2 mm·yr^{-1}, with the maximum uplift rate mainly occurring in the Western Alps (> 2 mm·yr^{-1}; Serpelloni et al., 2013, Nocquet et al., 2016). This high uplift rate cannot be explained simply by the ongoing convergence between the Adriatic microplate and the European Plate, nor can it be attributed solely to the postglacial rebound and erosion. Several studies have proposed that the present-day surface dynamics also are controlled by deep-seated processes (Serpelloni et al., 2013; Nocquet et al., 2016; Salimbeni et al., 2018; Sternai et al., 2019). Indeed, the elevation change in an orogenic belt has been dynamically controlled by the mantle convection at the edges of the converging plates (Faccenna and Becker, 2010). In the Mediterranean region, Faccenna et al. (2010) proposed that small-scale convection was the engine of the dynamic topography and microplate motions. Previous studies (Sue et al., 1999; Fox et al., 2015) have suggested that the high uplift and erosion rates may have been due to a surface response to slab breakoff under the Western Alps. However, this explanation has been questioned based on recent tomographic results, which have revealed a continuous high-velocity anomaly beneath the Western Alpine region that can be traced to the MTZ (Zhao et al., 2016a; Hua et al., 2017). Sternai et al. (2019) evaluated the relative contributions of the different velocity perturbation models (Lippitsch et al., 2003; Zhao et al., 2016a) to the observed vertical displacement rates at the surface and suggested that deglaciation and erosion account for about half of the observed uplift rate in the Western Alps. Regarding the mantle convection mechanism, although the absolute magnitude of its contribution to the uplift rate is difficult to independently evaluate based on existing knowledge, the mantle flow may have made a significant contribution of about 10–30% to the uplift rate at the orogen scale (Sternai et al., 2019) considering the velocity perturbation model by Zhao et al. (2016a).

With the subduction of the Alpine lithosphere, the downwelling of the lithospheric mantle into the deeper mantle may cause a return flow system, leading to mantle upwelling. We propose that the depression of the 410-km along the edge of the orogenic belt was the result of these small-scale mantle flows, which have transported hotter material from the MTZ into the upper mantle. Due to the lack of the toroidal flow between the northern end of the Apenninic subduction and the southwestern end of the Alpine subduction, the rollback of the Apenninic slab may have induced a suction effect and an asthenospheric counterflow around the northwestern part of the subducted European slab during the Neogene (Salimbeni et al., 2018; Malusà et al., 2021). We speculate that the vertical component of the mantle flow gradually propagated toward the southeast along the edge of the Alpine slab due to the suction effect caused by the rollback of the Apenninic slab (Fig. 7). Therefore, the mantle upwelling exhibited an oblique upward propagation path in the upper mantle (Figs. 6 and 7). In particular, Fig. 5f shows the good spatial agreement between the thinned area of the MTZ and the region of topographic uplift (green lines) under the constraint of this propagation path in the Western Alps. In addition to the upwelling from the MTZ, we noticed that the asthenosphere also was the source of the temperature increase in the external regions of the Western Alps Plate. Therefore, we suggested that the heat flow from the MTZ propagated upward, resulting in an increase in the temperature behind the Alpine slab. The low-velocity anomaly observed by the tomography results can be explained by such a thermal anomaly. When the upwelling reaches the bottom of the lithosphere at an estimated depth of 100 km (Lyu et al., 2017), it interacted with the overlying cold, dense mantle material, triggering surface uplift. This hypothesis can explain why the average elevation and the peaks of the Western Alps are higher than those of the other segments of the orogen, but further study is needed to verify this hypothesis. In addition to the occurrence of this phenomenon in the Western Alps, the contribution of a low-velocity anomaly behind the slab to the topographic uplift also was proposed in the Western United States by Bodmer et al. (2018, 2020). They proposed that a positive mantle buoyancy zone caused by local upwelling promoted the topographic uplift of the Cascadia Mountains by changing the slab dip or increasing the mechanical plate coupling.

5. Conclusions

We used 24904 high-quality RFs to investigate the topography of the MTZ discontinuities under the Western Alps and the surrounding areas. To obtain the absolute depths and improve the accuracy of the time-to-depth migrations, we used the 3-D EU60 velocity model to correct the ray paths and travel times in the upper mantle. We showed that the topographic relief of the two discontinuities was reduced by the correction for 3-D velocity heterogeneities. Compared with previous studies, our results confirmed that the thickening of the MTZ under the Western Alps cannot be solely attributed to the depression of the 660-km, and it also was caused by the uplift of the 410-km discontinuity. The uplifted 410-km may have been the result of the subduction of the Alpine slab to the depth of the upper MTZ, which provides an important constraint on the maximum present-day subduction depth of the Western Alps slab. As has been proposed in previous publications, the depression of the 660-km discontinuity may be linked to the remnants of oceanic lithosphere subducted during the closure of the Tethys Ocean. The most salient results of our study include the depression of the 410-km discontinuity and the thinning of the MTZ around the orogenic belt, which we attributed to a +120 K thermal anomaly caused by small-scale mantle upwelling. Due to the lack of uplift in the 660-km discontinuity, the possibility that the associated thermal anomaly originated from a mantle plume in the lower mantle can be excluded.

Our results indicated good agreement between the thinned area of the MTZ and the area of the observed topographic uplift, which we ascribed to a temperature increase promoted by mantle upwelling.

Acknowledgement

This research is funded by the National Natural Science Foundation of China (Grant 41625016, 41888101, and 91955210) and the National Key R&D Program of China (Grant No.2017YFC0601201). The data of the two CIFALPS project were provided by the data centers of the IGGCAS (Institute of Geology and Geophysics, Chinese Academy of Sciences) and the RESIF (French seismic and geodetic network). The data of the permanent stations were provided by the EIDA (European Integrated Data Archive). Most of them come from the Switzerland Seismological Network, RESIF, and other broadband permanent networks in metropolitan France, Regional Seismic Network of Northwestern Italy and Italian National Seismic Network. HY acknowledges the Western Australian Exploration Incentive Scheme (EIS). This is contribution xxx from the ARC Centre of Excellence for Core to Crust Fluid Systems (http://www.ccfs.mq.edu.au).

References

Agard, P., Handy, M.R., 2021. Ocean Subduction Dynamics in the Alps. Elements. 17, 101–108.

Bodmer, M., Toomey, D.R., Hooft, E.E.E., Schmandt, B., 2018. Buoyant asthenosphere beneath Cascadia influences megathrust segmentation. Geophys. Res. Lett. 45, 6954–6962.

Bodmer M, Toomey D.R., Roering J.J., Karlstrom L., 2020. Asthenospheric buoyancy and the origin of high-relief topography along the Cascadia forearc. Earth Planet. Sci. Lett. 531, 1–10.

Cottaar, S., Deuss, A., 2016. Large-scale mantle discontinuity topography beneath Europe: Signature of akimotoite in subducting slabs. J. Geophys. Res. Solid Earth 121, 279–292.

Deal, M.M., Nolet, G., van der Hilst, R.D., 1999. Slab temperature and thickness from seismic tomography: 1. Method and application to Tonga, J. Geophys. Res., 104 (B12), 28789–28802.

Dewey, J.F., Helman, M.L., Knott, S.D., Turco, E., Hutton, D.H.W., 1989. Kinematics of the western Mediterranean. Geol. Soc. (Lond.) Spec. Publ. 45, 265–283.

Dueker, K.G., Sheehan, A.F., 1998. Mantle discontinuity structure beneath the Colorado Rocky Mountains and high plains. Geophys. Res: Solid Earth, 103 (B4), 7153–7169.

Faccenna, C., Becker, T.W., 2010. Shaping mobile belts by small scale convection. Nature 465, 505–602.

Faccenna, C., Becker, T.W., Lallenmand, S., Lagabrielle, Y., Funiciello, F., Piromallo, C., 2010. Subduction-triggered magmatic pulses: A new class of plumes? Earth Planet. Sci. Lett. 299, 54–68.

Fox, M., Herman, F., Kissling, E., Willett, S.D., 2015. Rapid exhumation in the Western Alps driven by slab detachment and glacial erosion. Geology 43, 379–382.

Gao, S.S., Liu, K.H., 2014. Mantle transition zone discontinuities beneath the contiguous United States. J. Geophys. Res. Solid Earth 119, 6452–6468.

Handy, M.R., Schmid, S.M., Bousquet, R., Kissling, E., Bernoulli, D., 2010. Reconciling plate-tectonic reconstructions of Alpine Tethys with the geological-geophysical record of spreading and subduction in the Alps. Earth Sci. Rev. 102, 121–158.

Hua, Y., Zhao, D., Xu, Y., 2017. P wave anisotropic tomography of the Alps. J. Geophys. Res.

Solid Earth 122, 4509–4528.

Jacobsen, S.D., Smyth, J.R., 2006. Effect of water on the sound velocities of Ringwoodite in the transition zone. In: Jacobsen, S.D., van der Lee, S. (Eds.), AGU Monograph 168 "Earth's Deep Water Cycle", pp. 131–145.

Jolivet, L., Faccenna, C., 2000. Mediterranean extension and the Africa-Eurasia collision. Tectonics. 19, 1095–1106.

Katsura, T., Ito, E., 1989. The system Mg_2SiO_4-Fe_2SiO_4 at high pressures and temperatures: Precise determination of stabilities of olivine, modified spinel, and spinel. J. Geophys. Res. 94, 15663–15670.

Kennett, B.L.N., Engdahl, E.R., 1991. Traveltimes for global earthquake location and phase identification. Geophys. J. Int. 105, 429–465.

Koulakov, I., Kaban, M.K., Tesauro, M., Cloetingh, S., 2009. P and S velocity anomalies in the upper mantle beneath Europe from tomographic inversion of ISC data. Geophys. J. Int. 179(1), 345–366.

Ligorría, J.P., Ammon, C.J., 1999. Iterative deconvolution and receiver-function estimation. Bull. Seismol. Soc. Am. 89 (5), 1395 – 1400.

Lippitsch, R., Kissling, E., Ansorge, J., 2003. Upper mantle structure beneath the Alpine orogen from high-resolution teleseismic tomography. J. Geophys. Res. 108(B8), 2376.

Litasov, K. D., Ohtani, E., Sano, A., Suzuki, A., Funakoshi K., 2005. Wet subduction versus cold subduction. Geophys. Res. Lett. 32, L13312.

Liu, Z., Park, J., Karato, S., 2018. Seismic evidence for water transport out of the mantle transition zone beneath the European Alps. Earth Planet. Sci. Lett. 482, 93–104.

Lombardi, D., Braunmiller, J., Kissling, E., Giardini, D., 2009. Alpine mantle transition zone imaged by receiver functions. Earth Planet. Sci. Lett. 278 (3), 163–174.

Lustrino, M., Duggen, S., Rosenberg, C.L., 2011. The Central-Western Mediterranean: Anomalous igneous activity in an anomalous collisional tectonic setting. Earth Sci. Rev. 104, 1–40.

Lyu, C., Pedersen, H.E., Paul, A., Zhao, L., Solarino, S., the CIFALPS Working Group, 2017. Shear wave velocities in the upper mantle of the Western Alps: new constraints using array analysis of seismic surface waves. Geophys. Res. Lett. 210, 321–331.

Malusà, M.G., Faccenna, C., Baldwin, S.L., Fitzgerald, P.G., Rossetti, F., Balestrieri, M.L., Danišík, M., Ellero, A., Ottria, G., Piromallo, C., 2015. Contrasting styles of (U)HP rock exhumation along the Cenozoic Adria-Europe plate boundary (Western Alps, Calabria, Corsica). Geochem. Geophys. Geosyst. 16, 1786–1824.

Malusà, M.G., Anfinson, O.A., Dafov, L.N., Stockli, D.F., 2016. Tracking Adria indentation beneath the Alps by detrital zircon U-Pb geochronology: Implications for the Oligocene-Miocene dynamics of the Adriatic microplate. Geology 44(2), 155–158.

Malusà, M.G., Guillot, S., Zhao, L., Paul, A., Solarino, S., Dumont, T., Schwartz, S., Aubert, C., Baccheschi, P., Eva, E., Lu, Y., Pondrelli, S., Salimbeni, S., Sun, W., Yuan, H., 2021. The Deep Structure of the Alps Based on the CIFALPS Seismic Experiment: A Synthesis. Geochemistry, Geophysics, Geosystems. 22, e2020GC009466.

Nocquet, J.M., Sue, C., Walpersdorf, A., Tran, T., Lenôtre, N., Vernant, P., Cushing, M., Jouanne, F., Masson, F., Baize, S., Chéry, J., van der Beek, P.A., 2016. Present-day uplift of the western Alps. Sci. Rep. 6, 28404.

Paffrath, M., Friederich, W. and the AlpArray Working Group, 2020. Teleseismic P-wave travel time tomography of the Alpine upper mantle using AlpArray seismic network data, EGU General Assembly 2020, Online, 4 – 8 May 2020, EGU2020-13779.

Piromallo, C., Faccenna, C., 2004. How deep can we find the traces of Alpine subduction? Geophys. Res. Lett. 31, L06605.

Piromallo, C., Morelli, A., 2003. P wave tomography of the mantle under the Alpine-Mediterranean area. J. Geophys. Res. 108(B2), 2065.

Rawlinson, N., Sambridge, M., 2005. The fast marching method: an effective tool for tomographics imaging and tracking multiple phases in complex layered media. Exploration Geophysics 36, 341–350.

Salimbeni, S., Malusà, M.G., Zhao, L., Guillot, S., Pondrelli, S., Margheriti, L., Paul, A., Solarino, S., Aubert, C., Dumont, T., Schwartz, S., Wang, Q., Xu, X., Zheng, T., Zhu, R., 2018. Active and fossil mantle flows in the western Alpine region unravelled by seismic anisotropy analysis and high-resolution P wave tomography. Tectonophysics 731–732, 35–47.

Serpelloni, E., Faccenna, C., Spada, G., Dong, D., Williams, S.D., 2013. Vertical GPS ground motion rates in the Euro-Mediterranean region: new evidence of velocity gradients at different spatial scales along the Nubia-Eurasia plate boundary. J. Geophys. Res. 118, 6003–6024.

Schellart, W.P., 2004. Kinematics of subduction and subduction-induced flow in the upper mantle. J. Geophys. Res., Solid Earth 109 (b7), b07401.

Sternai, P., Sue, C., Husson, L., Serpelloni, E., Becker, T.W., Willett, S.D., Faccenna, C., DiGiulio, A., Spada, G., Jolivet, L., Valla, P., Petit, C., Nocquet, J.M., Walpersdorf, A., Castelltort, S., 2019. Present-day uplift of the European Alps: evaluating mechanisms and models of their relative contributions. Earth Sci. Rev. 190, 589–604.

Sue, C., Thouvenot, F., Fréchet, J., Tricart, P., 1999. Widespread extension in the core of the western Alps revealed by earthquake analysis. J. Geophys. Res. 104, 25611–25622.

Tarits, P., Hautot, S., Perrier, F., 2004. Water in the mantle: Results from electrical conductivity beneath the French Alps. Geophys. Res. Lett. 31, L06612.

Utada, H., Koyama, T., Obayashi, M., Fukao, Y., 2009. A joint interpretation of electromagnetic and seismic tomography models suggests the mantle transition zone below Europe is dry. Earth Planet. Sci. Lett. 281(3-4), 249–257.

van der Meijde, M., van der Lee, S., Giardini, D., 2005. Seismic discontinuities in the Mediterranean mantle. Phys. Earth Planet. Inter. 148, 233–250.

Wei, S.S., Shearer, P.M, 2017. A sporadic low-velocity layer atop the 410 km discontinuity beneath the Pacific Ocean. J. Geophys. Res. Solid Earth 122, 5144–5159.

Wood, B.J., 1995. The effect of H_2O on the 410-kilometer seismic discontinuity. Science 268, 74–76.

Yu, Y.G., Wentzcovitch, R.M., Tsuchiya, T., Umemoto, K., Weidner, D.J., 2007. First principles investigation of the postspinel transition in Mg_2SiO_4. Geophys. Res. Lett. 34, L10306.

Zhao, L., Paul, A., Guillot, S., Solarino, S., Malusà, M.G., Zheng, T.Y., Aubert, C., Salimbeni, S., Dumont, T., Schwartz, S., Zhu, R.X., Wang, Q.C., 2015. First seismic evidence for continental subduction beneath the Western Alps. Geology 43, 815–818.

Zhao, L., Paul, A., Malusà, M.G., Xu, X., Zheng, T., Solarino, S., Guillot, S., Schwartz, S., Dumont, T., Salimbeni, S., Aubert, C., Pondrelli, S., Wang, Q., Zhu, R., 2016a. Continuity of the Alpine slab unraveled by high-resolution P wave tomography. J. Geophys. Res. Solid

Earth 121, 8720–8737.

Zhao, L., Paul, A., Solarino, S., RESIF., 2016b. Seismic network YP: CIFALPS temporary experiment (China-Italy-France Alps seismic transect) [Data set]. RESIF - Réseau Sismologique et géodésique Français. https://doi.org/10.15778/RESIF.YP2012

Zhao, L., Paul, A., Solarino, S., RESIF., 2018. Seismic network XT: CIFALPS-2 temporary experiment (China-Italy-France Alps seismic transect #2 [Data set]. RESIF - Réseau Sismologique et géodésique Français. https://doi.org/10.15778/RESIF.XT2018

Zhu, H., Bozdag, E., Peter, D., Tromp, J., 2012. Structure of the European upper mantle revealed by adjoint tomography. Nature Geosci. 5, 493–498.

Zhu, H., Bozdag, E., Tromp, J., 2015. Seismic structure of the European upper mantle based on adjoint tomography. Geophys. J. Int. 201, 18–52.

Figures

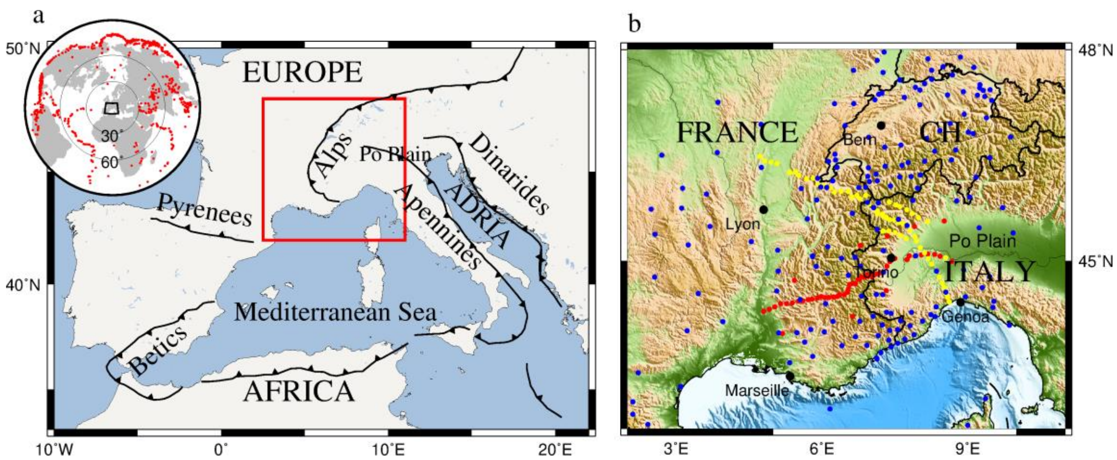

c

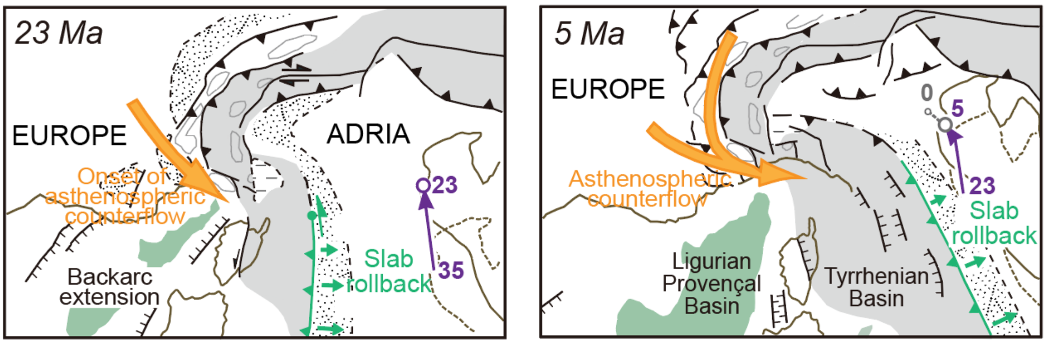

Fig. 1. (a) Tectonic sketch map of the Adria-Europe plate boundary zone. The red box indicates the area in frame b. Small inset. Locations of the 1182 teleseismic events used in this study. (b) Map showing the distribution of the seismic stations used in this study. The red and yellow dots represent the temporary stations of CIFALPS and CIFALPS-2, respectively. The blue dots represent the 193 permanent broadband stations. CH: Switzerland. (c) Neogene evolution of the Alpine and Apenninic subductions (simplified after Malusà et al., 2021). The gray areas denote the Alpine metamorphic wedge and the Apenninic accretionary wedge; the purple arrows indicate the Adria trajectories relative to Europe in the given time interval (in Ma) (from Dewey et al., 1989); and the orange arrows indicate the direction of the asthenospheric counterflow.

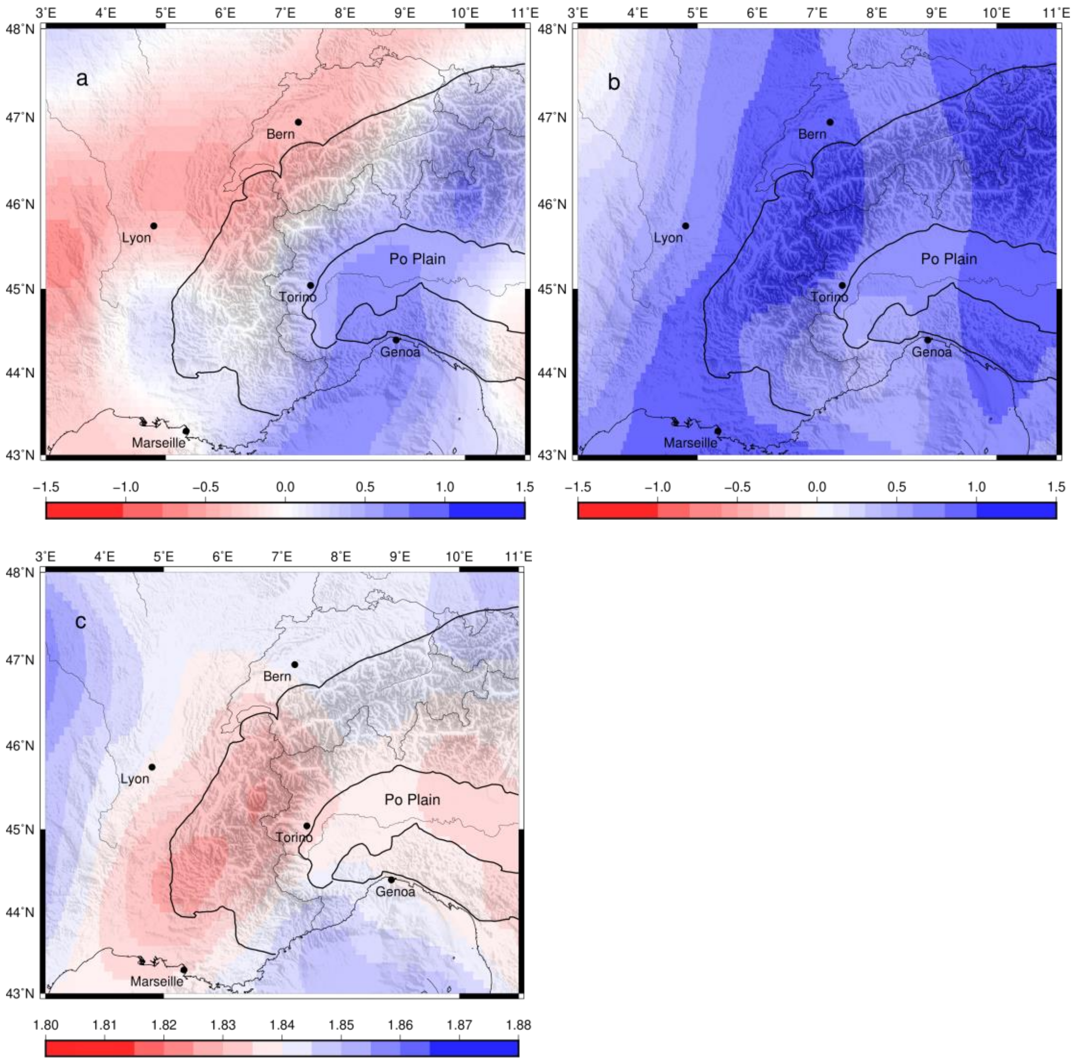

Fig. 2.Variations in P-wave velocity (percentages regarding the regional average) at depths of (a) 410 km and (b) 660 km extracted from the EU60 model. (c) Vp/Vs ratio at depth of 600 km calculated from the absolute P-wave and S-wave velocities of the EU60 model (Zhu et al., 2015). The thin black lines are the major tectonic boundaries.

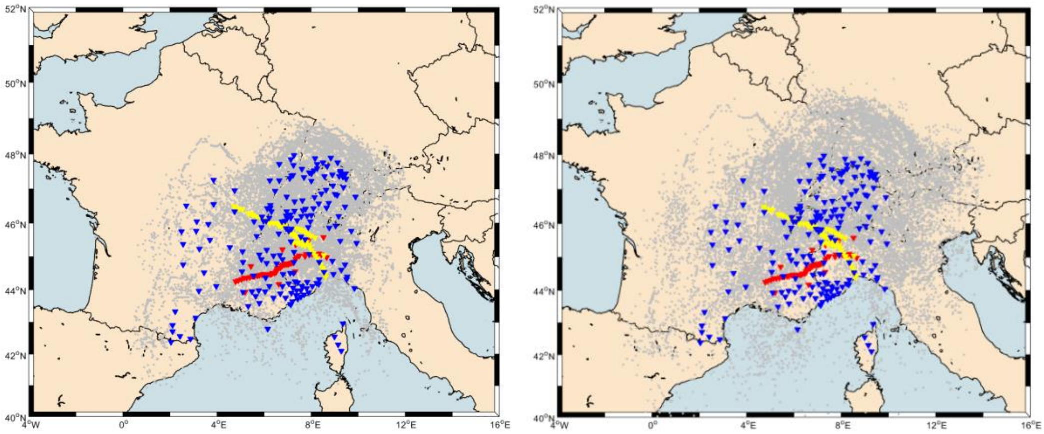

Fig. 3. Maps of ray piercing points at depths of (a) 410 km and (b) 660 km computed using the 3-D velocity model. The triangles represent the 307 broadband seismic stations. The blue triangles are the 197 stations of the French (FR, RD, G) and Italian (IV, GU) permanent networks. The red and yellow triangles represent the temporary stations of the CIFALPS and CIFALPS-2 projects, respectively.

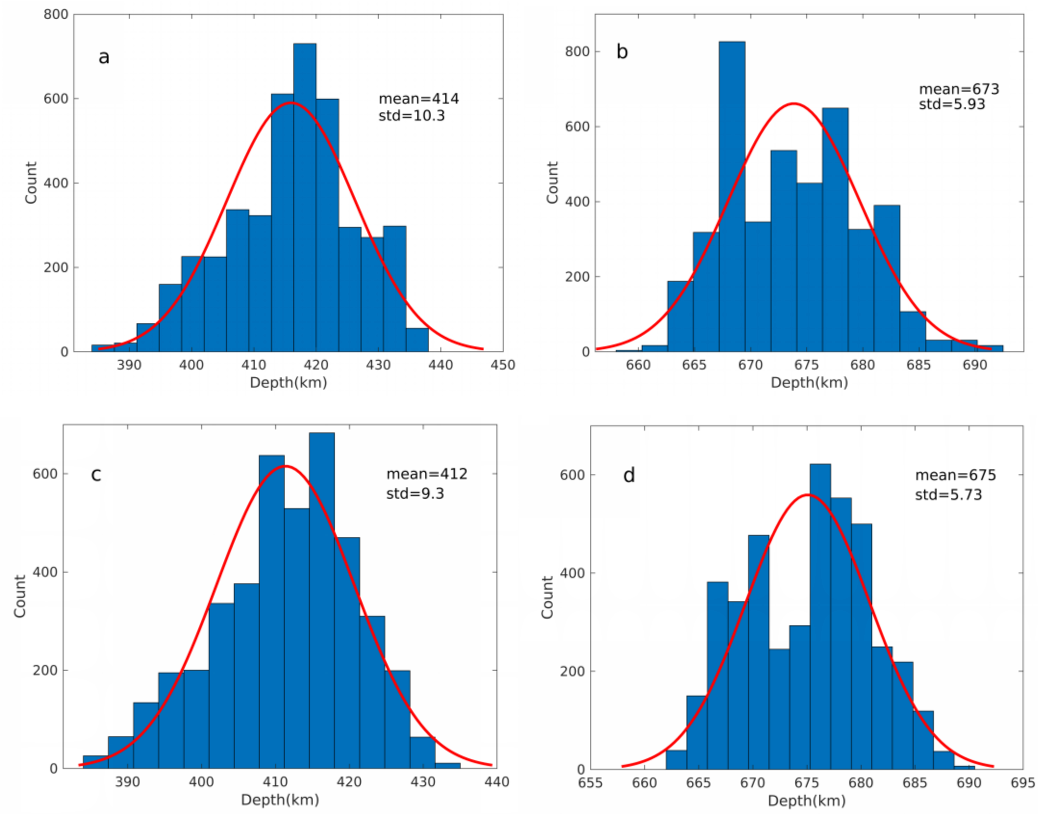

Fig. 4. Distribution of the depth picks of the 410-km discontinuity between 390 and 430 km based

on (a) the IASP91 model, and (c) the EU60 model. Distribution of the depth picks of the 660 km discontinuity between 640 and 710 km based on (b) the IASP91 model and (d) the EU60 model. The best fit normal distribution is indicated by a red line. The average depth and standard deviation are indicated (km) in the upper right corner of each panel.

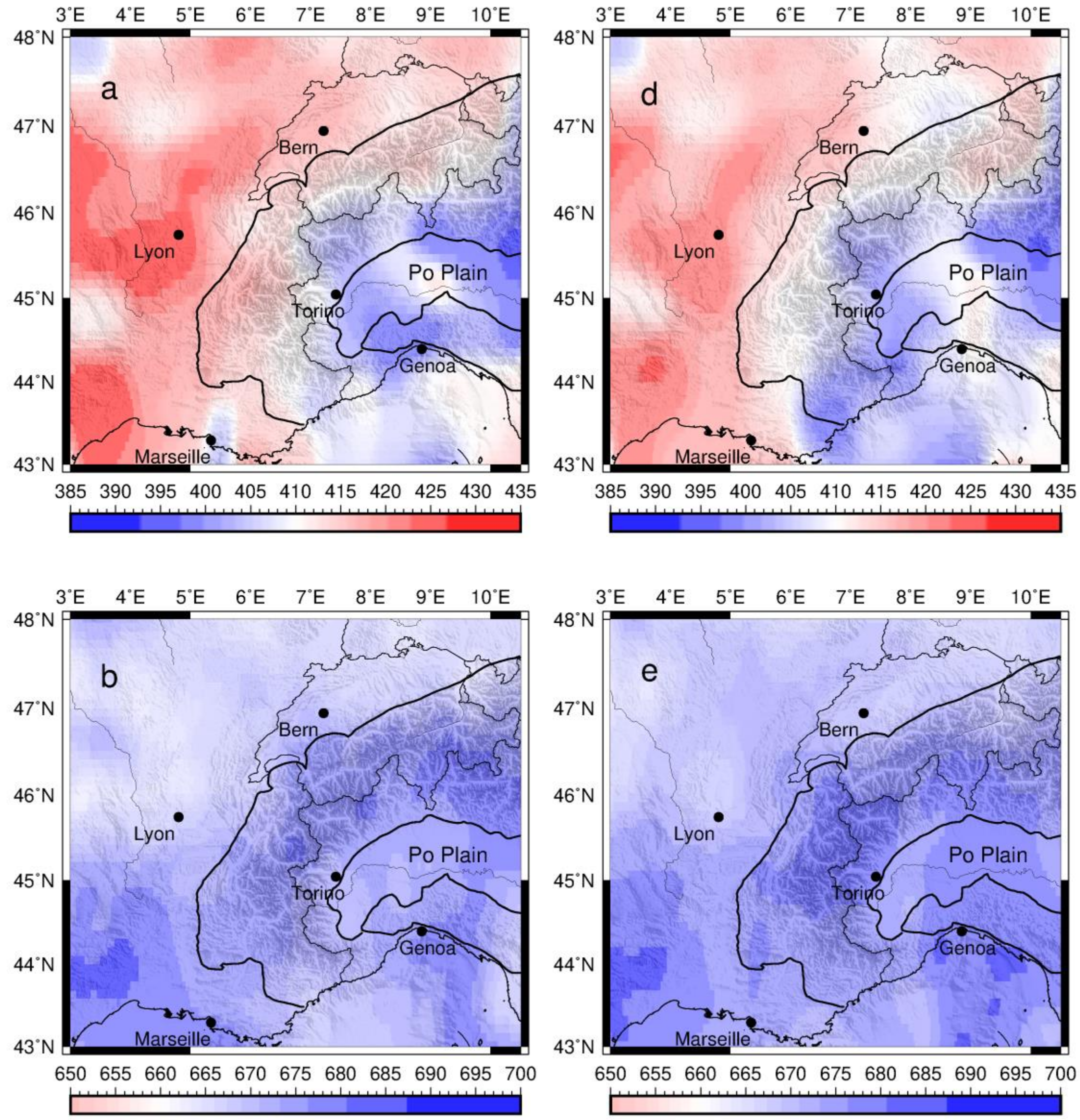

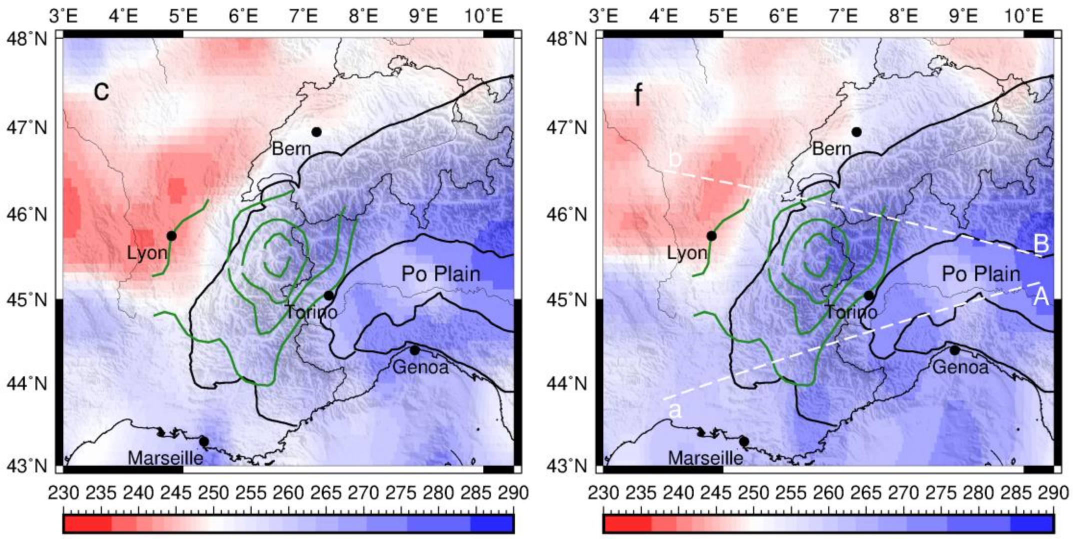

Fig. 5. Maps of the depths of the mantle discontinuities and thickness of the MTZ from data migrated using the IASP91 model: (a) 410-km discontinuity, (b) 660-km discontinuity, and (c) thickness of the MTZ, and from data migrated using the EU60 model (d), (e), and (f), as in (a–c). The green lines show the contours of the strong present-day surface uplift rates (Nocquet et al., 2016). The white dashed lines in (f) refer to Fig. 6.

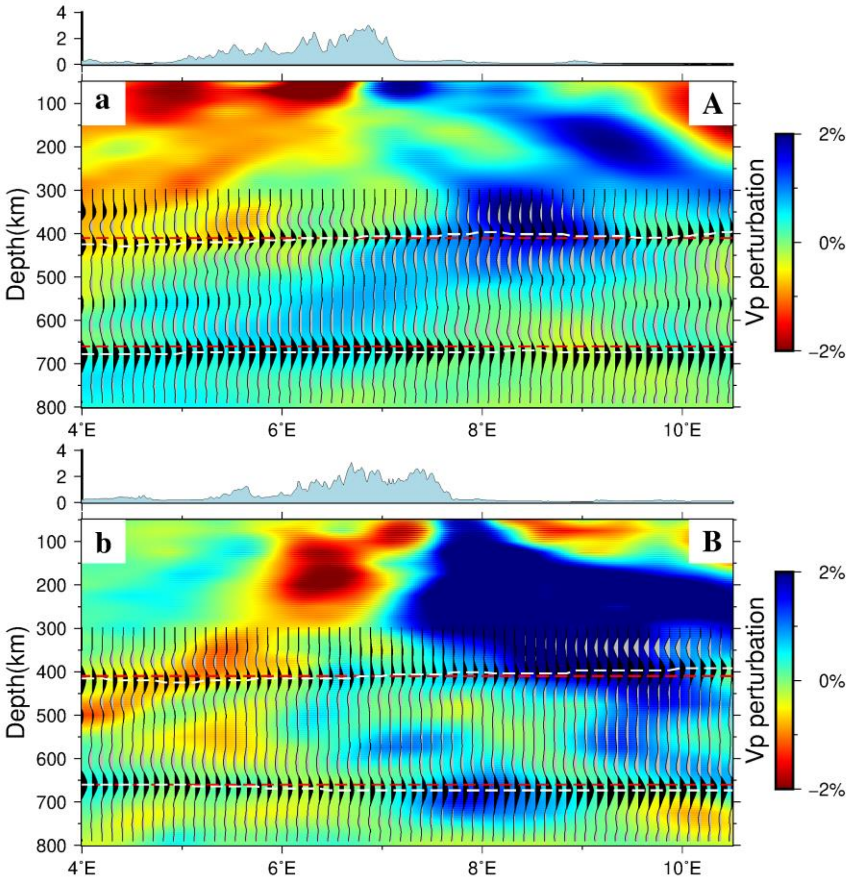

Fig. 6. Cross sections through the CCP receiver-function stack with 3-D velocity corrections. The locations of the sections are shown in Fig. 5f. The background is the P-wave velocity perturbation model of Zhao et al. (2016a). The red dashed lines denote the reference depths of 410 and 660 km, and the depths of the maximum amplitudes for the P410s and P660s are indicated by the white dashed lines.

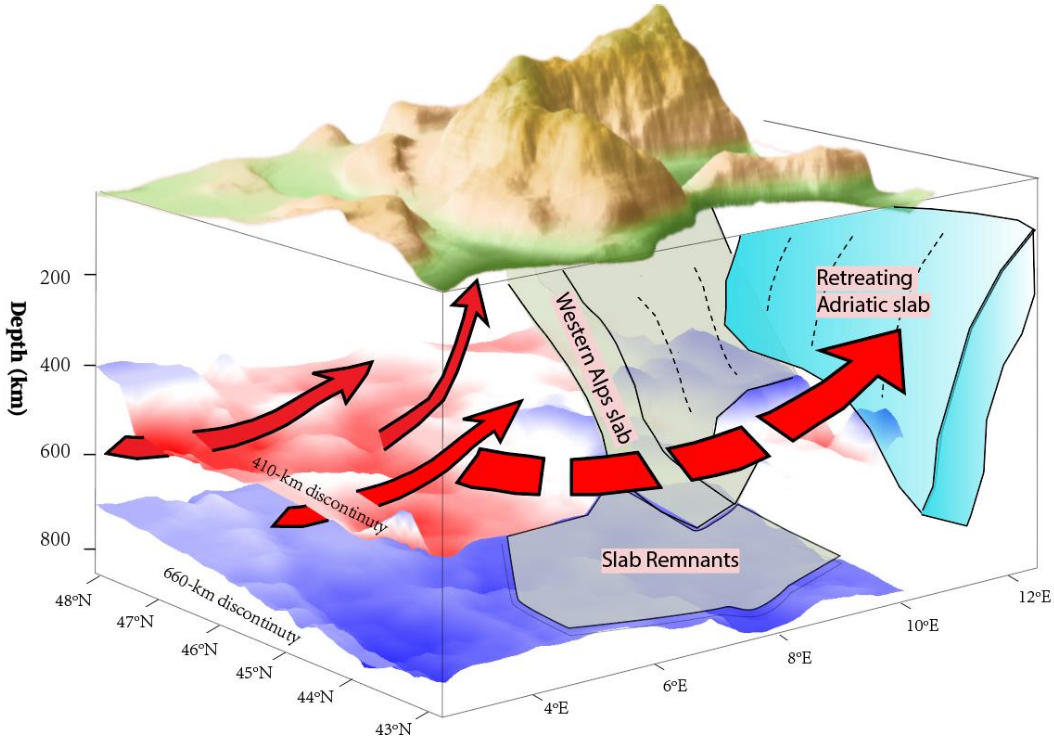

Fig. 7. A 3-D scheme illustrating the proposed structure and dynamic processes in the upper mantle beneath the Western Alps according to our observations, the seismic tomography results by Zhao et al. (2016), and the anisotropy results by Salimbeni et al. (2018). The uplifted 410-km discontinuity (blue area at longitudes of >6°E) indicates that the subducted plate has passed through the 410-km discontinuity and entered the MTZ. The depression of the 660-km discontinuity may be related to remnants of subducted oceanic lithosphere. The depressed 410-km discontinuity (red area) may be related to a thermal anomaly induced by small-scale mantle upwelling (represented by red arrows), which may have been triggered by downwelling of the Alpine lithosphere and affected by the rollback of the Apenninic slab to the south.

Figures

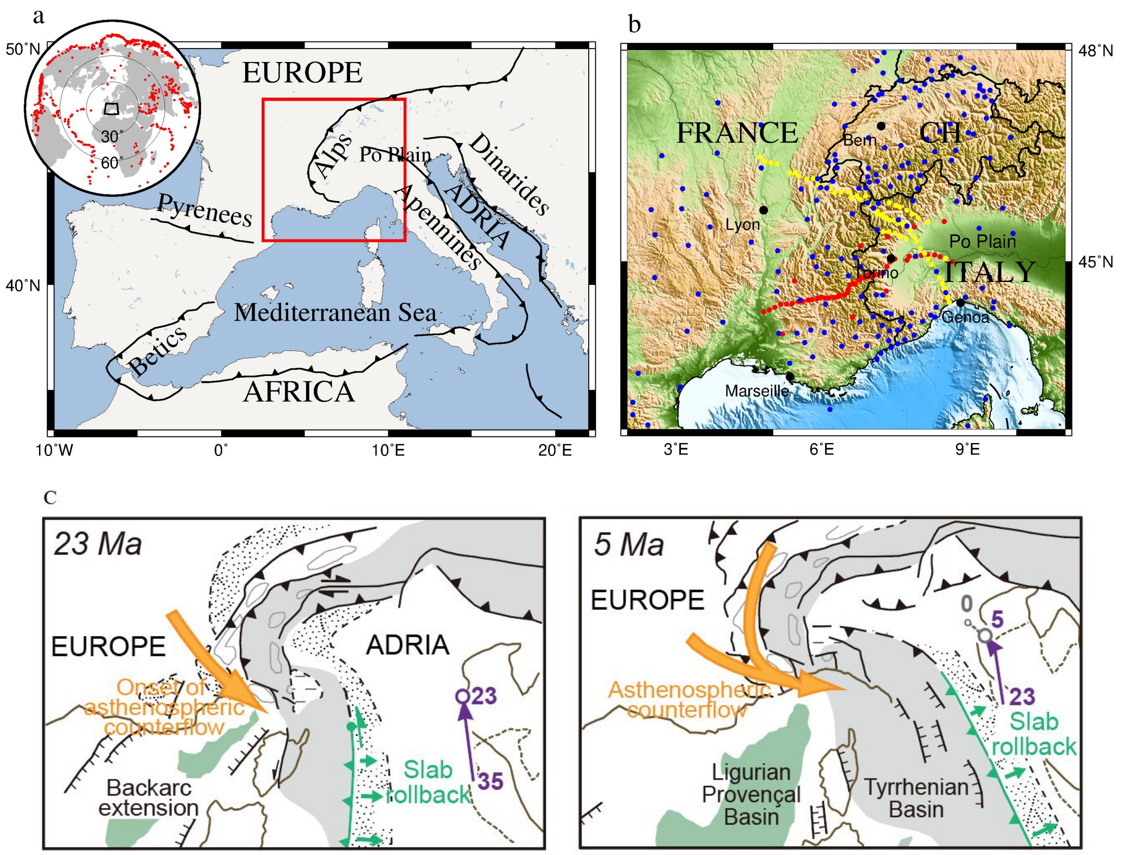

Fig. 1. (a) Tectonic sketch map of the Adria-Europe plate boundary zone. The red box indicates the area in frame b. Small inset. Locations of the 1182 teleseismic events used in this study. (b) Map showing the distribution of the seismic stations used in this study. The red and yellow dots represent the temporary stations of CIFALPS and CIFALPS-2, respectively. The blue dots represent the 193 permanent broadband stations. CH: Switzerland. (c) Neogene evolution of the Alpine and Apenninic subductions (simplified after Malusà et al., 2021). The gray areas denote the Alpine metamorphic wedge and the Apenninic accretionary wedge; the purple arrows indicate the Adria trajectories relative to Europe in the given time interval (in Ma) (from Dewey et al., 1989); and the orange arrows indicate the direction of the asthenospheric counterflow.

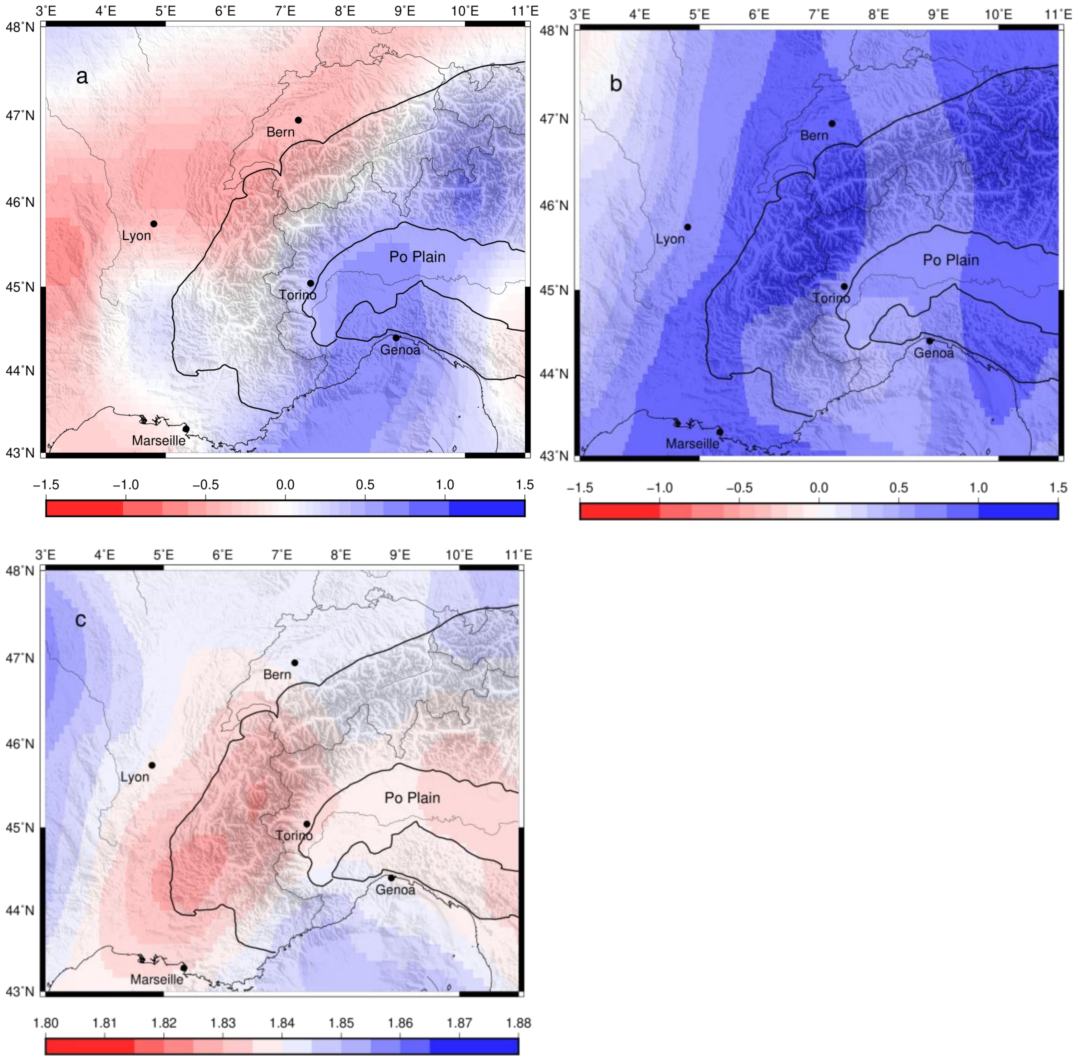

Fig. 2.Variations in P-wave velocity (percentages regarding the regional average) at depths of (a) 410 km and (b) 660 km extracted from the EU60 model. (c) Vp/Vs ratio at depth of 600 km calculated from the absolute P-wave and S-wave velocities of the EU60 model (Zhu et al., 2015). The thin black lines are the major tectonic boundaries.

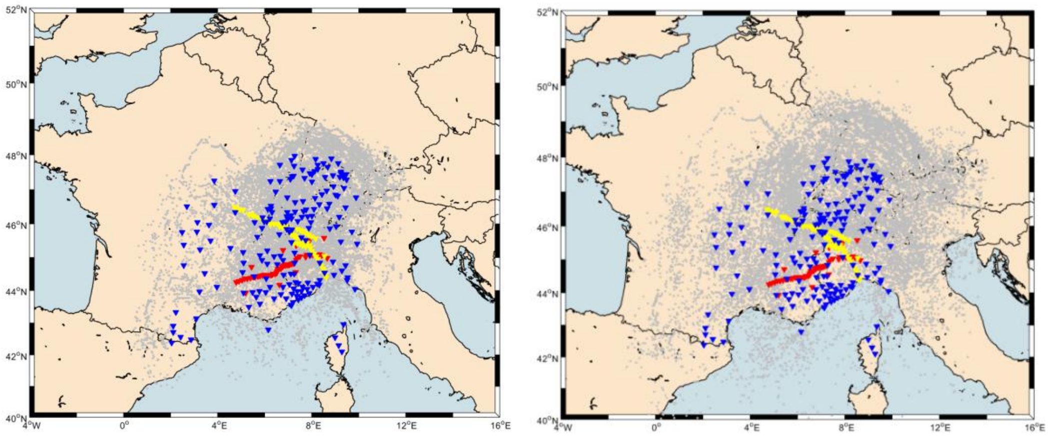

Fig. 3. Maps of ray piercing points at depths of (a) 410 km and (b) 660 km computed using the 3-D velocity model. The triangles represent the 307 broadband seismic stations. The blue triangles are the 197 stations of the French (FR, RD, G) and Italian (IV, GU) permanent networks. The red and yellow triangles represent the temporary stations of the CIFALPS and CIFALPS-2 projects, respectively.

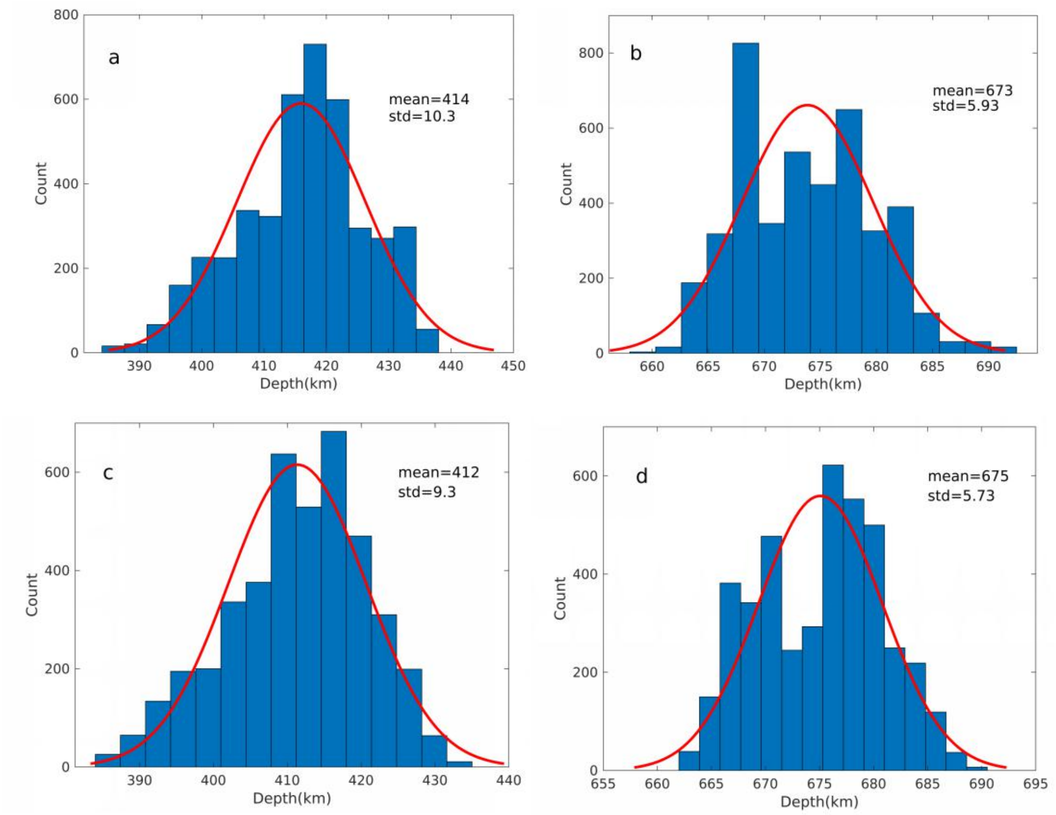

Fig. 4. Distribution of the depth picks of the 410-km discontinuity between 390 and 430 km based on (a) the IASP91 model, and (c) the EU60 model. Distribution of the depth picks of the 660 km

discontinuity between 640 and 710 km based on (b) the IASP91 model and (d) the EU60 model. The best fit normal distribution is indicated by a red line. The average depth and standard deviation are indicated (km) in the upper right corner of each panel.

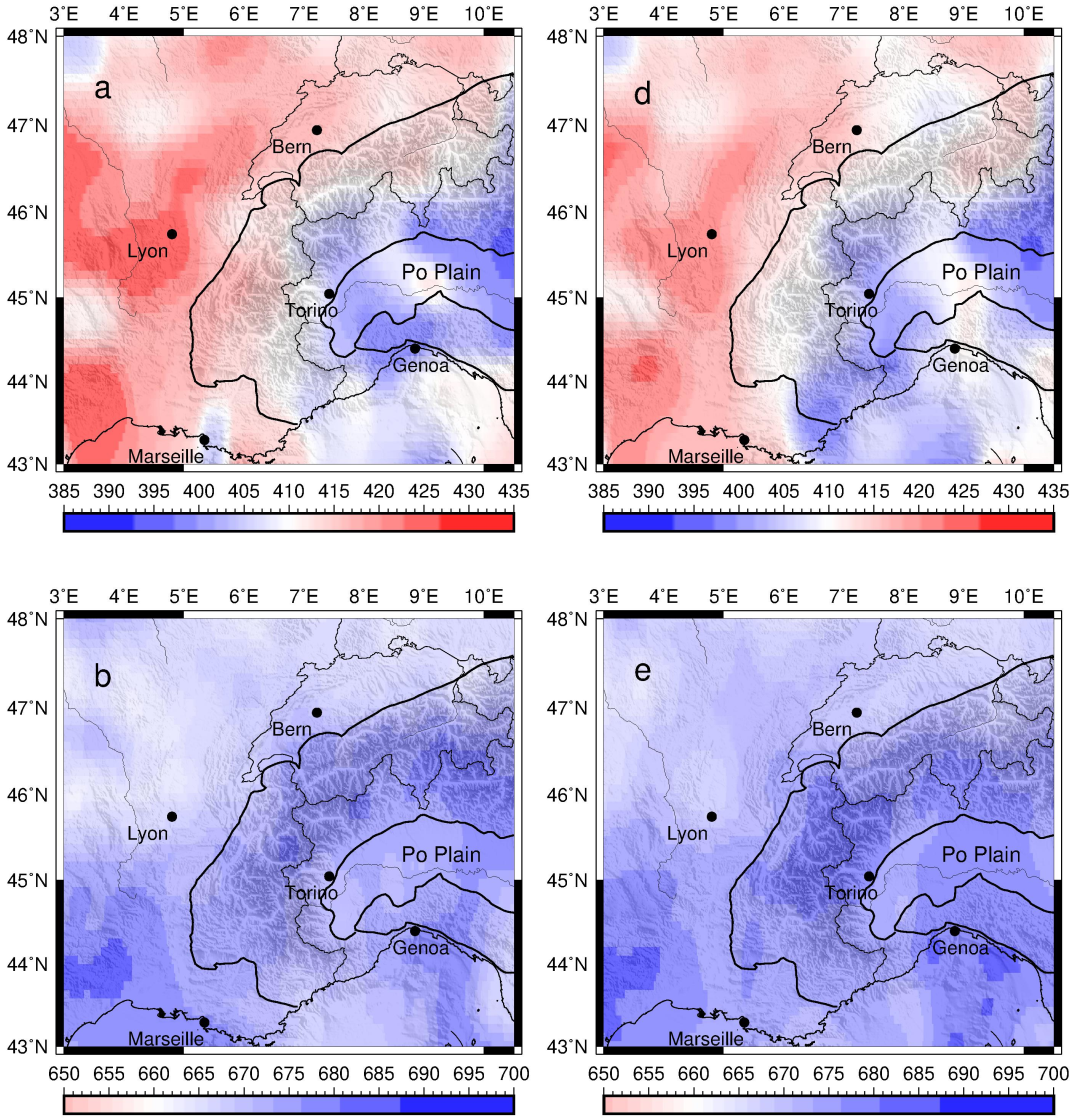

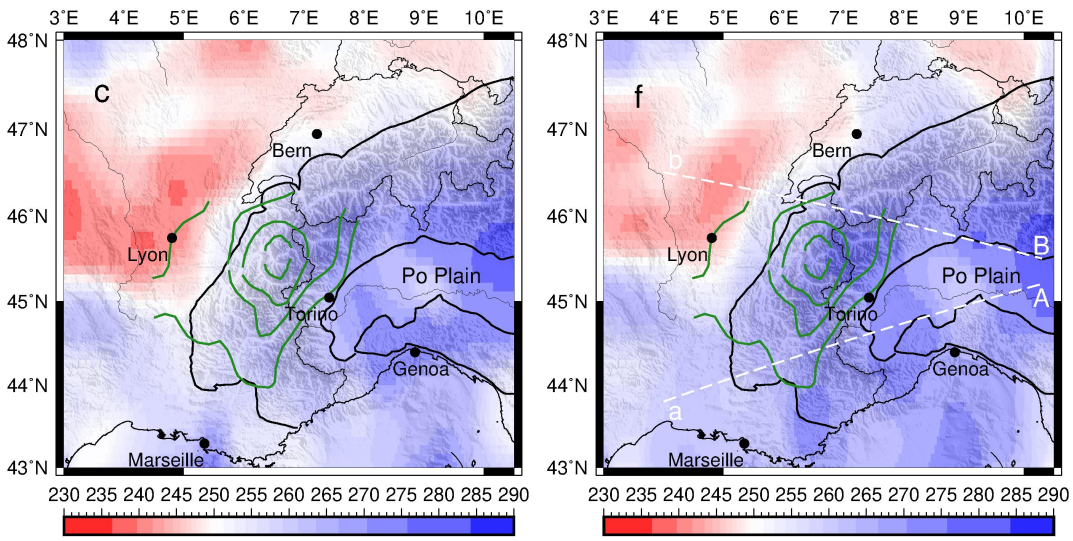

Fig. 5. Maps of the depths of the mantle discontinuities and thickness of the MTZ from data migrated using the IASP91 model: (a) 410-km discontinuity, (b) 660-km discontinuity, and (c) thickness of the MTZ, and from data migrated using the EU60 model (d), (e), and (f), as in (a–c). The green lines show the contours of the strong present-day surface uplift rates (Nocquet et al., 2016). The white dashed lines in (f) refer to Fig. 6.

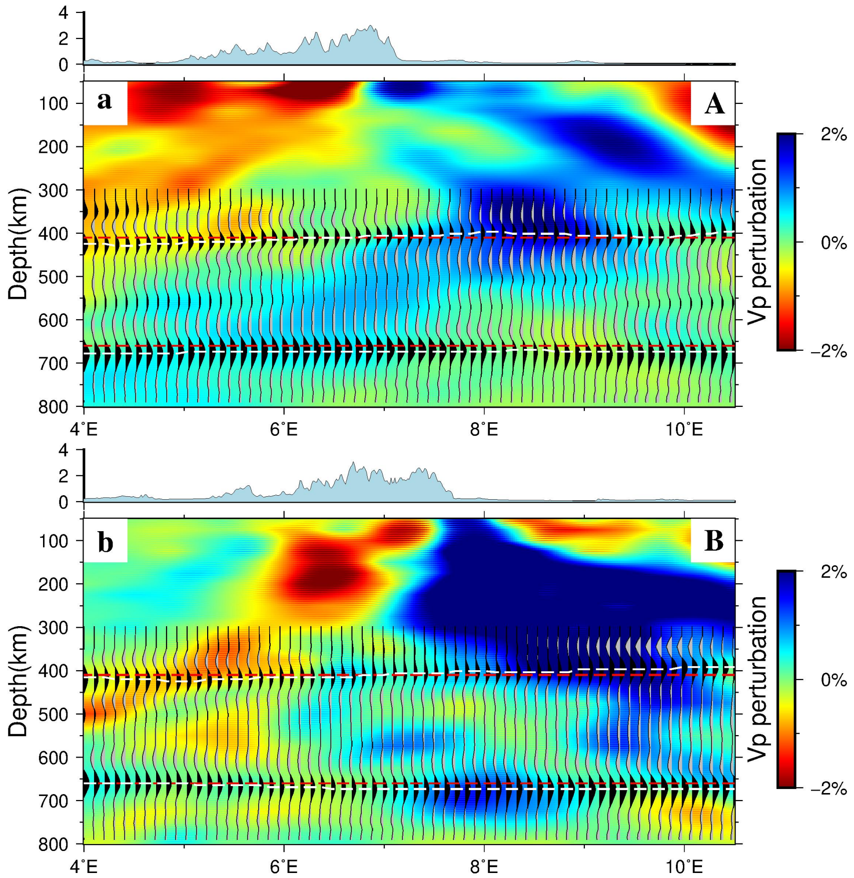

Fig. 6. Cross sections through the CCP receiver-function stack with 3-D velocity corrections. The locations of the sections are shown in Fig. 5f. The background is the P-wave velocity perturbation model of Zhao et al. (2016a). The red dashed lines denote the reference depths of 410 and 660 km, and the depths of the maximum amplitudes for the P410s and P660s are indicated by the white dashed lines.

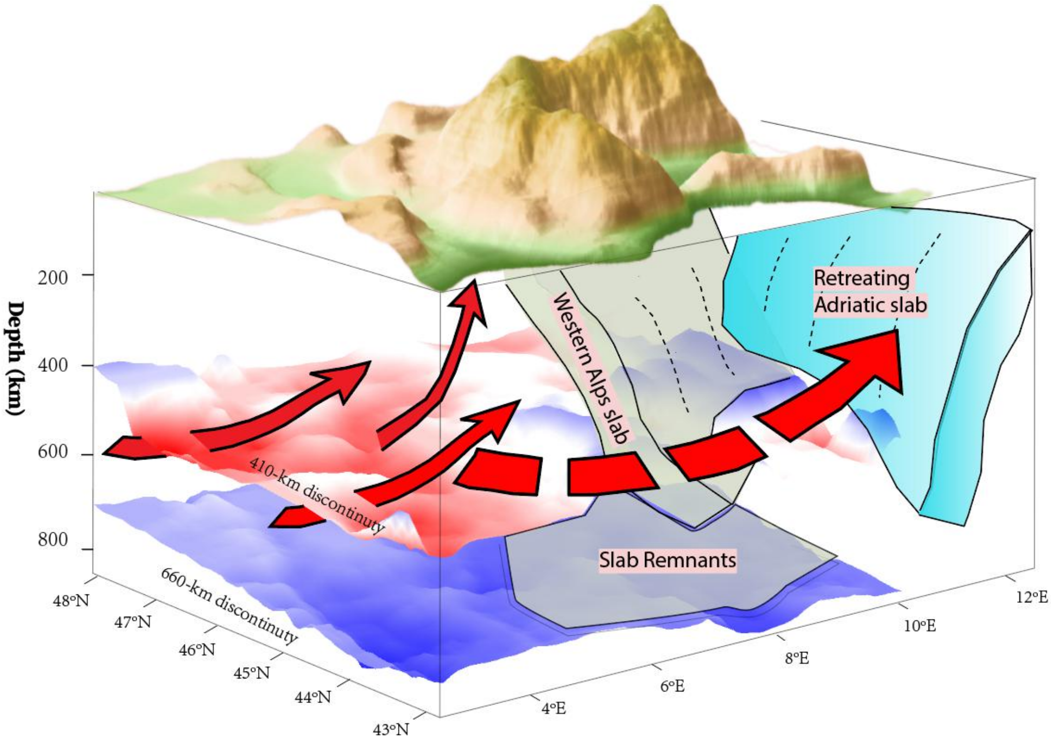

Fig. 7. A 3-D scheme illustrating the proposed structure and dynamic processes in the upper mantle beneath the Western Alps according to our observations, the seismic tomography results by Zhao et al. (2016), and the anisotropy results by Salimbeni et al. (2018). The uplifted 410-km discontinuity (blue area at longitudes of >6°E) indicates that the subducted plate has passed through the 410-km discontinuity and entered the MTZ. The depression of the 660-km discontinuity may be related to remnants of subducted oceanic lithosphere. The depressed 410-km discontinuity (red area) may be related to a thermal anomaly induced by small-scale mantle upwelling (represented by red arrows), which may have been triggered by downwelling of the Alpine lithosphere and affected by the rollback of the Apenninic slab to the south.